Supplementary material for “Gigahertz-rate-switchable wavefront shaping through integration of metasurfaces with photonic integrated circuit”

Haozong Zhong,[a, †] Yong Zheng, [a, †] Jiacheng Sun, [b, †] Zhizhang Wang, [b] Rongbo Wu, [a] Ling-en Zhang, [a] Youting Liang, [a] Qinyi Hua, [a] Minghao Ning, [a] Jitao Ji, [b] Bin Fang, [c] Lin Li, [a, e, *] Tao Li, [b, *] Ya Cheng, [a, d, e, *] Shining Zhu [b, *]

[a]State Key Laboratory of Precision Spectroscopy, School of Physics and Electronic Science, East China Normal University, Shanghai 200241, China

[b]National Laboratory of Solid State Microstructures, College of Engineering and Applied Sciences, Nanjing University, Nanjing, 210093, China

[c]College of Optical and Electronic Technology, China Jiliang University, Hangzhou 310018, China

[d]State Key Laboratory of High Field Laser Physics and CAS Center for Excellence in Ultra-Intense Laser Science, Shanghai Institute of Optics and Fine Mechanics (SIOM), Chinese Academy of Sciences (CAS), Shanghai 201800, China

[e]Collaborative Innovation Center of Extreme Optics, Shanxi University, Taiyuan 030006, China

*****Lin Li, lli@lps.ecnu.edu.cn; Tao Li, taoli@nju.edu.cn; Ya Cheng, ya.cheng@siom.ac.cn; Shining Zhu, zhusn@nju.edu.cn

S1: The amplitude and phase evolution in the slab waveguide

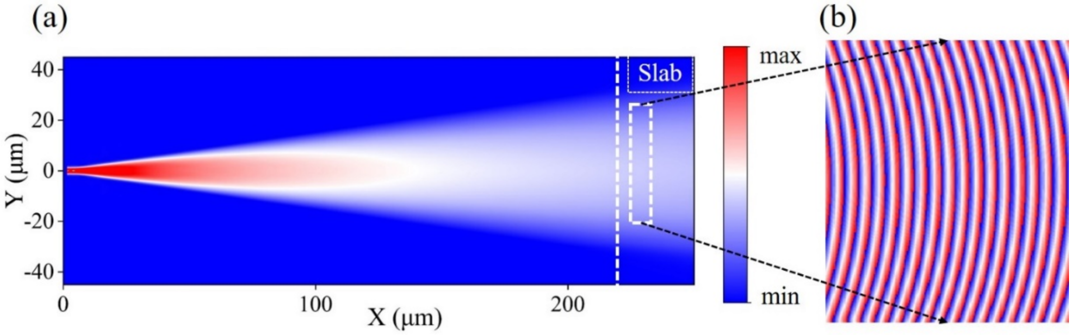

Figure S1. (a) Simulated amplitude evolution associated with the guided mode in the taper and slab waveguide. (b) The phase evolution in slab waveguide.

Here, we present the variations in amplitude and phase of waveguide mode during its propagation from an adiabatic taper to a planar waveguide. Figure S1(a) illustrates the process, where light travels from a single mode ridge waveguide to a slab waveguide through an adiabatic taper of 200 μm. The mode size gradually increases to 60 μm, further enlarging within the slab waveguide, resulting in a region of uniform amplitude. In this case, the width at the end of taper is 60 μm. By designing the length and width of the taper, the area of uniform amplitude can be further optimized. Figure 1(b) illustrates the phase evolution of light within the slab waveguide, presenting an arc-shaped phase profile. Fitting results indicate that the center of the arc corresponds to the starting point of the taper. Although the arcs have very large radii of curvature, they can be approximated as near planar waves within a limited area. Based on the simulation result, the precise polarization states distribution, which formed by the superposition of the two orthogonally propagated waveguide modes, could be retrieved. The functionalities in the main text are also designed based on the simulated amplitude and phase evolution, taking into account the non-planar nature of the waveguide modes.

The slab waveguide mode will travel a relatively long distance within the device before it reaches the boundary of the waveguide after passing through the metasurface. Meanwhile, the waveguide mode in the slab gradually expands after passing through the tapers as illustrated in Figure S1. (a). Consequently, following the long-distance propagation, when the light encounters the boundary and is reflected back, the intensity of the guided mode light will be significantly attenuated. In addition, the design of the metasurface relies on the wavefront and the propagation direction of the waveguide mode, while the reflected light dose not consistent with them. As a result, the influence of the reflected light on the performance of the device can be safely disregarded.

S2: Design of polarization dependent guided-wave-driven metasurface

Once we obtain the amplitude and phase evolution in the planar waveguide for the two orthogonally propagated channels, we can extract the actual distribution of identical polarizations ψ on the waveguide. These distributions appear as a series of lines, similar to the dashed lines shown in Fig. 3(a) in the main text. The polarization state can be dynamically modulated to any desired state by adjusting the voltages applied to the electrodes of the MZI and the phase shifter.

Without loss of generality, here we take LCP state as the reference design polarization as an example. By considering the phase evolution, we can also identify a series of arcs with the same phase (as shown in Fig. S1(b)). These arcs, together with the lines of identical polarization, form an array of crosses, where the metasurface nanostructures will be located. To achieve the desired beam (beam 1), the metasurfaces are designed to fulfill the corresponding phase and amplitude distributions based on the LCP state. Simultaneously, another array of crosses can be obtained by introducing a phase difference of π to the previous series of arcs, and aligning them with the lines of identical polarization. We can design a separate metasurface to generate a different beam (beam 2) based on the right circularly polarized (RCP) state.

When the polarization of the lines is adjusted to be LCP, only beam 1 can be formed, while only beam 2 can be formed when the polarization is adjusted to be RCP. It is worth noting that the choice of the reference design polarization can be arbitrary, as discussed in the main text.

S3: The polarization extinction ratio of the generated beam

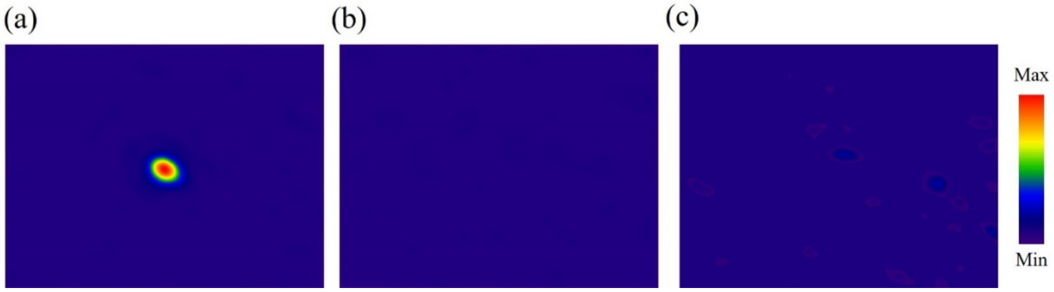

Figure S2. (a) The cross-section image of the focal spot in Figure 2(c) at *X*-*Y* plane. (b) The corresponding image after performing polarization analyzing at the orthogonal polarization state. (c) The recorded image with increased exposure time by twenty times.

We performed measurements to determine the polarization extinction ratio (PER) of the focal point. In Fig. S2(a), we show a cross-sectional image of the focal spot in Fig. 2(c) in the main text at the X-Y plane. Fig. S2(b) displays the corresponding image after polarization analysis at the orthogonal state. It can be observed that the focal spot disappears after polarization filtering. To retrieve the energy of the spot under this condition, we increased the exposure time of the camera by a factor of twenty. The resulting image is presented in Fig. S2(c), where the focal spot is not visible, indicating a high degree of polarization purity. Let P1 and P2 represent the integrated intensities of the two focal positions in Figure S2(a) and Figure S2(c), respectively. The PER of the focal spot can be calculated using the formula $10 * \log_{10}((20 * P1) / P2)$. The calculated value is 20.79 dB, indicating a minimum PER of 20 dB for the focal spot.

S4 Calculation of the propagation process of scattered light

This section introduces the calculation of the propagation of electromagnetic waves using the Huygens-Fresnel principle. According to this principle, each point on a wavefront can be regarded as a secondary wave source. By superimposing the amplitudes and phases of these secondary wave sources, the wavefront at the next moment can be obtained. In the calculation, each metasurface structure is treated as a point source. The initial amplitudes and phases of these point sources are determined by considering the simulated data of individual nanostructures and the propagation conditions of the waveguide mode. Based on the principles of the Huygens-Fresnel principle, the distribution of the light field in surrounding space can be derived with these point sources.

S5: Simulation of individual element of guided-wave-driven metasurface

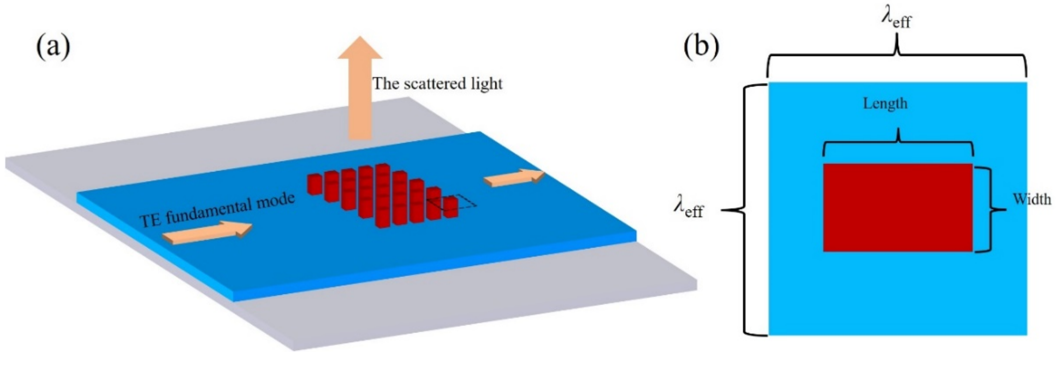

Figure S3. (a) Simulation schematic of metasurface structure of different sizes. (b) Schematic of a unit cell of the metasurface.

Different from the simulation method for the unit cell of metasurface in free space, the periodic boundary condition cannot be directly applied to the guided-wave-driven metasurface. In order to accurately evaluate the scattering performance of the nanostructure, we employed a 5x5 metasurface array arranged on a waveguide for convenient simulation. It is observed that the amplitude and phase of the scattered light do not exhibit significant variations in larger arrays. The period of the array is chosen to match the effective wavelength of the waveguide mode, allowing for near-plane scattering. The waveguide width is set to 10μm to create a mode spot area large enough to accommodate the TE fundamental mode. This ensures that the entire array operates within a region of uniform amplitude. By varying the length and width of the nanostructures within the range of 100nm to 500nm, we obtained the intensity and phase of the scattered light associated with the corresponding nanostructures interacting with the waveguide mode.

S6: Optical measurement setups

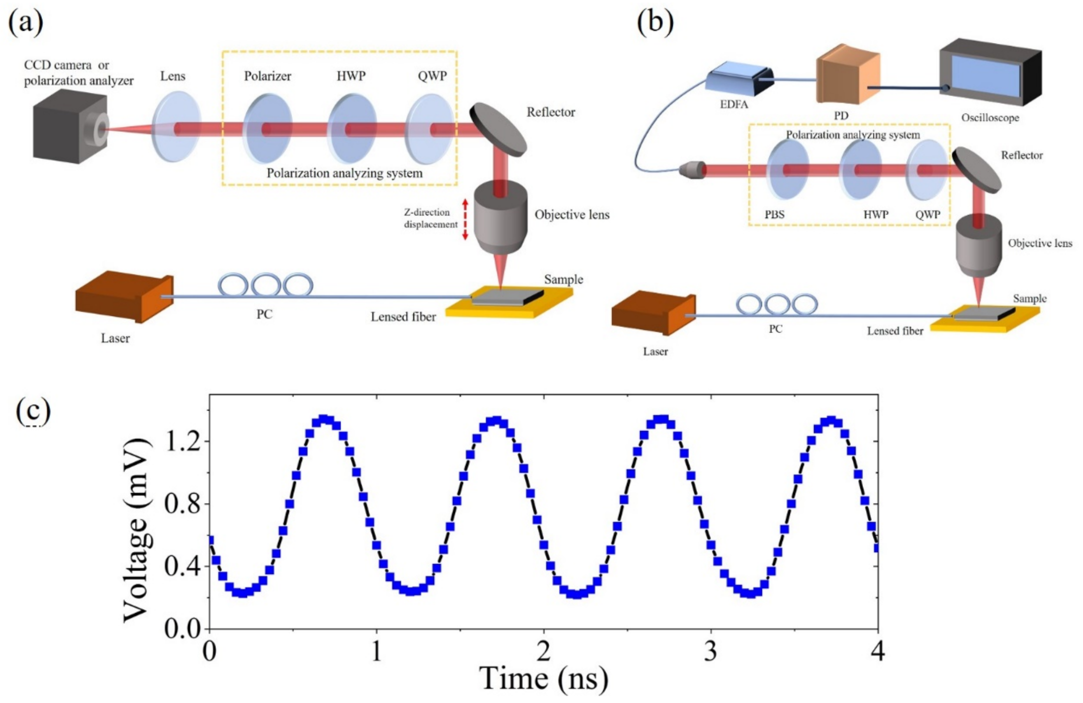

Figure S4. (a) The optical measurement setup to image the scattered light from the device. (b) The optical measurement system to characterize the modulation performance. The optical components within the yellow dashed box represent the polarization analysis system, which can be removed when polarization analysis is not required. (c) The test result under modulation by a 1 GHz sinusoidal voltage signal.

Figure S4(a) illustrates the measurement setup, where a 1550 nm laser passes through a polarization controller and is coupled to the waveguide on the sample via a single-mode fiber lens. The scattered light from the metasurface is collected by an objective lens and then imaged with a CCD camera. The objective lens is mounted on a high-precision translation stage for z-direction displacement. By gradually adjusting the translation stage along z-direction, the images are captured at different heights and subsequently overlapped to reconstruct a three-dimensional stereoscopic image.

Meanwhile, this setup can be utilized for polarization state characterization. For this purpose, an polarization analyzing system is employed before the CCD camera. To characterize the of polarization reconfigurable performance of the device at high speed, the CCD camera is replaced with a high-speed Avalanche Photodiode (Thorlabs, APD430C/M, DC - 400 MHz). By adjusting the quarter waveplate and polarizer, precise derivation of the Stokes parameters is achieved [56]. In addition, the polarization state is characterized using a commercial polarization analyzer (PA) (Thorlabs PAX1000IR2/M) for lower modulation speeds and longer measurement durations.

Figure S4(b) illustrates the experimental setup employed for characterizing the high-speed modulation performances. The light emitted by the metasurface is coupled into a fiber and amplified using an Erbium-Doped Fiber Amplifier (EDFA). Subsequently, the light is detected by a high-speed photon detector (FINISAR XPDV21x0(RA)). Finally, the optoelectronic detector's signal is collected by an oscilloscope (Tektronix MSO64B). Figure S4(c) illustrates the test result under modulation by a 1 GHz sinusoidal voltage signal. To examine the polarization properties of the modulated light, a set of polarization analyzing systems can be added before the coupling system, as depicted in the figure.

S7：Analysis of the Performance of the Polarization State Reconfiguration

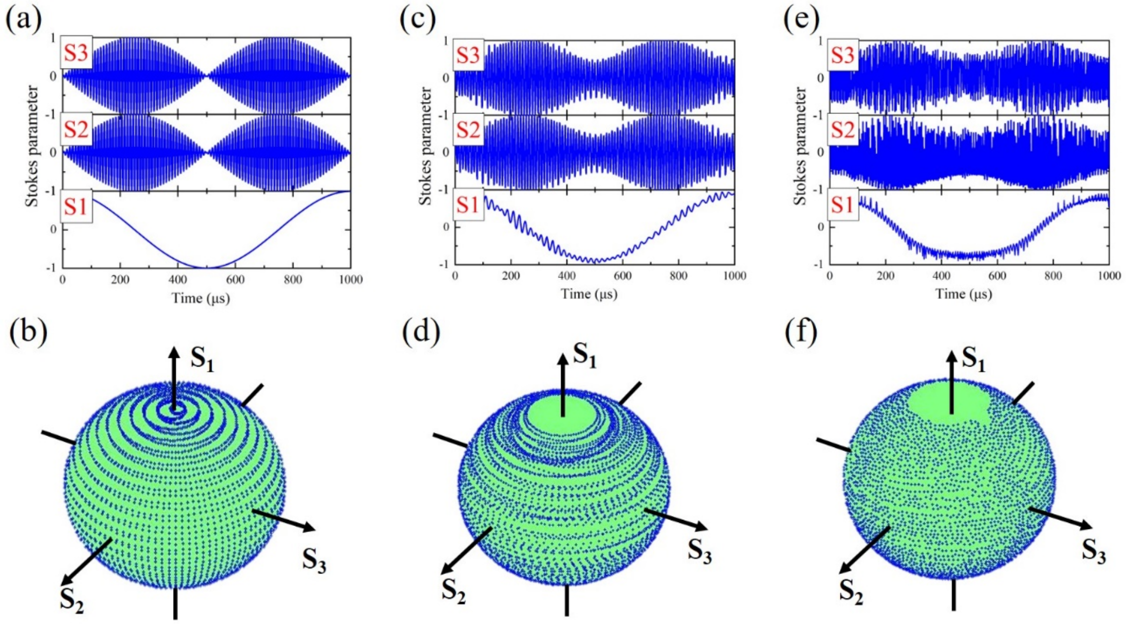

Figure S5. (a) Theoretical analysis of time-varying Stokes parameters when applying triangle wave signals with frequencies of 1 kHz and 100 kHz to the electro-optic phase shifters, respectively, and (b) the corresponding polarization states' distributions on the Poincaré sphere. (c) Theoretical analysis of time-varying Stokes parameters considering uneven splitting ratio in the directional coupler, and (d) the corresponding polarization states' distributions on the Poincaré sphere. (e) The measured Stokes parameters as a function of time when applying the two triangle wave signals to the phase shifters, respectively, and (f) the corresponding polarization states' distributions on the Poincaré sphere. Here the blue dots represent the polarization states of the focal spot.

In order to assess the performance of the polarization reconfiguring with our device, two triangle wave signals with frequencies of 1 KHz and 100 KHz are applied to the electrodes of the Mach-Zehnder interferometer (MZI) and phase shifter, respectively. In this scenario, the optical electrical field of the two guided waves can be expressed as follows [34]:

$$\begin{pmatrix}|\mathrm{a}\rangle\\|\mathrm{b}\rangle\end{pmatrix} = C_{\varphi} \times C_{\mathrm{DC}} \times C_{\theta} \times C_{\mathrm{DC}} \times \begin{pmatrix}|1\rangle\\0\end{pmatrix} \tag{S1}$$

where C_{DC}, C_θ and C_φ are the transfer matrices of directional couplers, first and second phase shifters, respectively. $|1\rangle$ is the input optical electrical field. $|\mathrm{a}\rangle$ and $|\mathrm{b}\rangle$ represent optical electrical field of the two guided waves at the tapers, corresponding to the relevant portion of Equation (1) in the main text:

$$|\mathrm{a}\rangle + |\mathrm{b}\rangle = \begin{bmatrix} Ae^{i\varphi_x} \\ Be^{i\varphi_y} \end{bmatrix} \tag{S2}$$

Figure S5. (a) shows theoretical analysis of time-varying Stokes parameters when applying triangle wave signals with frequencies of 1 kHz and 100 kHz to electro-optic phase shifters, with ideal 1:1 splitting ratio in the directional couplers. However, the splitting ratio of the directional couplers is difficult to reach 1:1 due to the fabrication imperfections. Additionally, the waveguides here support higher order modes, which could be excited with the fiber lenses in the waveguide mode coupling process. These higher order modes will impact the reconfigurated polarizations of the focal spot, though their intensities are much weaker than the fundamental mode. Figure S5. (c, d) present the theoretically calculated results after taking these factors into account. Here, we assume a splitting ratio of 5:4 between the two ports of the directional coupler, and a ratio of 10:1 between the fundamental mode and higher order modes. The results show that these two factors significantly impact the Stokes parameters, and the polarization states cannot fully cover the surface of the Poincaré sphere. Figure S5. (e, f) displays the experimentally measured Stokes parameters and the corresponding reconfigured polarization states of the focus on the Poincaré sphere. The distribution of the polarization states agrees with the theoretical analysis in Figure S5. (c,d). Further development will be addressed in the future work to improve the performance. An additional electrically controlled interferometer can be introduced to improve the splitting ratio and make the reconfigured polarization state fully cover the Poincaré sphere. Meanwhile, stratagems to filter out high-order modes can be involved to reduce the impact of high order modes.

S8: The efficiency of the device

The out-of-plane extraction efficiency of the integrated metasurface is quantified as the ratio of the optical power carried by the generated beams to the optical power within the input guided waves. Under these prescribed conditions, we conducted numerical simulations to the metasurfaces depicted in Figures 2. (b), Figures 3. (b) and Figures 5. (c), to assess their efficiency. The results indicate efficiencies of 0.2%, 6%, and 11% respectively. In experimental endeavors, the overall efficiency is contingent upon the coupling efficiency between the fiber lens and the waveguide mode, the propagation loss of LN waveguide, and the out-of-plane extraction efficiency of the metasurface. Specifically, the coupling efficiency between the fiber lens and the waveguide mode was quantified at about -7dB. The propagation loss within the LN waveguide is of a magnitude low enough to be negligibly significant. As a result, the overall efficiency of the devices is estimated to be approximately 0.04%， 1.2% and 2.2% [50, 55]. The overall efficiency can be further increased by optimizing the geometric parameters of the metasurfaces, the underneath waveguide and the coupling method between the fiber mode and the waveguide mode.

S9: Fabrication methods

Our device is fabricated on a 4-inch X-cut LNOI wafer. It is composed of a 500 nm-thick LN layer bonded to a buried silica (SiO_2) layer on a silicon support substrate with a thickness of 500 μm. The fabrication process involved the utilization of Photolithography Assisted Chemo-Mechanical Etching (PLACE) technology for photonic integrated circuits (PICs) [57].

The fabrication process of PIC comprises four main steps. Firstly, a 600 nm-thick chromium (Cr) film is deposited onto the surface of the LNOI substrate using magnetron sputtering. Subsequently, the Cr film on the LNOI sample is patterned into the waveguide mask utilizing a space-selective femtosecond laser system (PHAROS, LIGHT CONVERSION Inc.). Following that, a chemo-mechanical polishing (CMP) process is employed to selectively etch the thin film of lithium niobate using a wafer polishing machine (UNIPOL802, Kejing Inc.). In this step, the lithium niobate thin film, protected by the Cr mask, remains intact after the CMP process and served as the waveguides. Finally, the fabricated structure is immersed in a chromium etching solution to remove the Cr mask.

After completing the LN waveguide fabrication, two layers of LOR5B film and AZ5214 film are spin-coated on the sample. Subsequently, an ultraviolet (UV) exposure is conducted to define the electrode patterns. After the development process, a 300 nm-thick gold film is deposited onto the wafer. Then, a lift-off process is employed to transfer the patterns.

Following the electrode fabrication, a layer of α-Si is deposited on the chip using plasma-enhanced chemical vapor deposition (PECVD). Subsequently, the metasurface patterns are written on an electron beam resist (PMMA) through electron beam lithography (EBL). After development, a lift-off process is employed to define the chromium pattern and served as a hard mask for the following dry etching process. The α-Si pattern is transferred afterwards by dry etching process with a mixture of C4F8 and SF6 plasma (HSE200, Naura) and a remove of Cr hard mask [50].